Materials Advances

ROYAL SOCIETY OF CHEMISTRY

PAPER

View Article Online
View Journal | View Issue

Cite this: *Mater. Adv.*, 2024, 5, 336

A novel triphenylamine based push–pull fluorophore bearing a 2-thiohydantoin unit for toxic Hg^{2+} ion detection: exploring its potential for live cell imaging†

Pratiksha P. Gawas,[a] Buthanapalli Ramakrishna,[b] Rajesh Pamanji,[c] Joseph Selvin[c] and Venkatramaiah Nutalapati *[a]

A novel fluorescent chemosensor (**TPA-2TH**) containing triphenylamine (TPA) appended in conjugation with 2-thiohydantoin (2TH) is developed and confirmed by various analytical techniques like FT-IR spectroscopy, NMR spectroscopy, HR-MS and single crystal X-ray diffraction (SC-XRD). The crystal structure analysis revealed a propeller-shaped TPA unit and a co-facial herringbone packing arrangement stabilized by N–H···S, N–H···O and C–H···O in the crystal lattice. **TPA-2TH** exhibited a strong absorption band at ~431 nm and emitted a yellow-green fluorescence at λ_{max} = 522 nm in THF, attributed to an efficient charge-separated state resulting from ICT between TPA and 2TH. A solvatochromic effect was observed with a red shift in the emission wavelength as the polarity of the solvent increased. **TPA-2TH** showed unprecedented selectivity with *turn-off* fluorescence upon complexation with diamagnetic Hg^{2+} ions, attributed to an increase in the spin–orbit coupling and a weakened ICT effect caused by Hg^{2+} binding. The addition of Hg^{2+} to **TPA-2TH** resulted in the formation of a 2 : 1 complex (**TPA-2TH**–Hg^{2+}), confirmed by the coordination of a sulphur atom of **TPA-2TH** with Hg^{2+} ions, as evidenced by ^{1}H NMR spectroscopy and Job's plot analysis. A linear relationship between the fluorescence intensity of **TPA-2TH** and the concentration of Hg^{2+} ions is observed with a LOD of 3.3 pM. Furthermore, the toxicological effect of **TPA-2TH** is explored in zebrafish larvae and embryos to provide a sensitive bio-indicator for metal ion contamination and fluorescence imaging. This comprehensive approach combining fluorescence quenching and behavioural toxicity assessment offers a practical method for evaluating metal ion contamination and its potential toxic effects on aquatic organisms with acute behavioural toxicity end points using adult zebrafish.

Received 17th August 2023,
Accepted 16th November 2023

DOI: 10.1039/d3ma00559c

rsc.li/materials-advances

1. Introduction

Donor–Acceptor (D–A) organic molecules with π-conjugated structures possessing electron-rich donor (D) groups linked to an acceptor (A) through an olefinic core have attracted interest from academic and technological researchers for decades. However, this is still a highly active area of research focused on the development of novel organic molecules with interesting properties like enhanced charge transfer (CT), tunable energy levels, broad absorption and emission spectra, high charge mobility, nonlinear optical properties, enhanced light-harvesting efficiency, thermal stability and processing ability. These intriguing properties of D–A molecules make them highly sought-after in the scientific community, driving on-going research and exploration into their synthesis, characterization and application in a wide range of fields like in developing solvatochromic probes,[1–4] nonlinear optics,[5] chemosensors,[6–8] electro-optics,[9,10] photochromic[11] and piezo-chromic materials[10] and as active layers in photovoltaics.[12,13]

In a D–A system, the intramolecular charge transfer (ICT) character depends on the HOMO–LUMO (highest occupied and lowest unoccupied molecular orbital) gap, so that its optical properties can be tailored in three ways, *i.e.* (i) incorporating different donor and acceptor units and assuring efficient

[a] *Functional Materials Laboratory, Department of Chemistry, Faculty of Engineering and Technology, SRM Institute of Science and Technology, Kattankulathur, Tamil Nadu 603203, India. E-mail: nvenkat83@gmail.com, venkatrv1@srmist.edu.in*
[b] *Division of Chemistry, Vellore Institute of Technology (VIT), Chennai, Tamil Nadu, 632014, India*
[c] *Department of Microbiology, Pondicherry University, Puducherry, 605014, India*

† Electronic supplementary information (ESI) available. CCDC 2278085. For ESI and crystallographic data in CIF or other electronic format, see DOI: https://doi.org/10.1039/d3ma00559c

interactions between them, (ii) extension and spatial arrangement of the π-bridge and (iii) planarization of the entire molecule.[14–16] Hence, modifying the structure of donors along with the acceptor unit offers the possibility of tuning their electronic and photophysical properties. D–A molecules have been extensively used as chemical sensors due to their tunable photophysical properties. In the excited states, D–A molecules display the ICT phenomenon. Changes in the surrounding microenvironment can quickly alter the CT properties. In chemosensors, the acceptor/donor unit is the recognition site that binds to metal ions resulting in the perturbation of the ICT state. The subsequent electronic effects are reflected as changes in the wavelength maxima of the absorption and fluorescence spectra of the D–A system. Huang's group developed a D–A–D system for visual Hg^{2+} ion detection that consists of an ethynyl unit connected to the center of a naphthyridine molecule by two di(hydroxyethyl)aniline moieties at the terminal.[17] Debdas *et al.* reported on a dimethyaminophenyl and diazine-based D–A system for Ag^{+} ion detection.[18] Sreejith and co-workers reported a D–A–D based fluorophore interconnected through a vinylic bridge for ratiometric sensing and imaging of Zn^{2+} ions in biological media.[19] Thilagar *et al.* designed and developed a fluorophore using triphenylamine (TPA) as a donor connected to two different acceptor groups, *i.e.*, BODIPY and diaryl boryl, on either side, which exhibited two characteristic ICT states showing the corresponding absorption at different energy levels.[20] Many potential colorimetric and fluorescent Hg^{2+} ion chemosensors have been reported.[7,21–41] However, developing a simple probe that can monitor global contaminants like hazardous metal ions,[23–29] toxic anions, biomolecules,[42–44] *etc.* at permissible levels remains challenging. Generally, the Hg^{2+} ion prefers to coordinate with ligands that have nitrogen, oxygen or sulphur atoms. 2TH has the ability to act as a chelator for cations, enabling the detection of various anthropogenic molecules and ions. This capability is due to the presence of sulphur and nitrogen atoms in the 2TH ring.[45] It contains both amide and thioamide groups, which act as both proton acceptors and donors. This structural feature allows for the formation of diverse hydrogen bonding networks in its crystal structure.[45,46] As a result of our interest in designing and developing a new fluorescence sensor, we have developed a TPA and 2TH based chemosensor (**TPA-2TH**) with TPA as a donor and the 2TH unit acting as an Hg^{2+} ion chelator and acceptor. In this report, we aim to develop a novel **TPA-2TH** molecular probe through Knovenagel condensation between TPA aldehyde and 2TH. The synthesized **TPA-2TH** is found to be highly fluorescent, showing distinct quenching in fluorescence upon complexation with diamagnetic Hg^{2+} ions. Hg^{2+} binding to **TPA-2TH** would decrease the electron-donating ability of TPA, thus weakening the ICT effect in the fluorophore. This fluorescent probe exhibited excellent solvatochromic behaviour, high selectivity, high sensitivity and fluorescence change response towards Hg^{2+}. Furthermore, toxicological studies of **TPA-2TH** are caried out to apply it as a bio-indicator for metal ion contamination using zebrafish larvae and embryos as a model system along with acute behavioural toxicity end points using adult zebrafish.

2. Experimental section

2.1 Chemicals and materials

All chemicals were purchased from Sigma Aldrich and the solvents used were of AR grade. Double distilled water obtained from a MilliQ system (>18.2 MΩ) was used in the spectroscopic study. All experiments involving zebrafish for the purpose of live cell imaging were conducted in compliance with relevant laws and institutional guidelines (PU/IAEC/2023-24/314). The experimental protocols were approved by Pondicherry University, which oversees and ensures the ethical treatment of animals in research. Efforts were also made to minimize the number of fish used during the course of the experiments.

2.2 Measurements

FT-IR (Fourier-transform infrared) spectra were recorded using a Shimadzu IR Tracer-100 in the ATR mode. ^{1}H and ^{13}C NMR spectra were recorded on a Bruker 500 MHz spectrometer, whereas the chemical shifts (δ) and coupling constants (J) were reported in parts per million (ppm) and Hz, respectively. ESI-MS spectra were acquired using a 6230B Time of Flight (TOF) system, Agilent technology. Single-crystal X-ray experiments were performed on an Oxford Xcalibur (Mova) diffractometer equipped with an EOS CCD detector and a microfocus sealed tube using Mo Kα radiation (λ = 0.71073 Å). Data collection was made at 100 K and the structure is solved using SHELXS,47 and OLEX2 (version 1.2)[48,49] was used to solve and refine the crystal structures. All non-hydrogen atoms were refined anisotropically. Hydrogen atoms on heteroatoms were located from difference electron density maps, and all C–H atoms were fixed geometrically using the HFIX command. The WinGX package was used for final refinement, production of CIFs and the crystallographic table, and Oak Ridge Thermal Ellipsoid Plot-3 (ORTEP-3) was used for structure visualization and making the molecular representations. The packing diagram was analyzed using Mercury 2020.2.0. The Hirshfeld analysis was performed using Crystal Explorer 21.5.[50] Thermogravimetric analysis (TGA) was carried out on an SDT Q600 thermal analyzer under a nitrogen atmosphere at a heating rate of 10 °C min^{-1}. Differential scanning calorimetry (DSC) of the compounds was carried out with a DSC 214 Polyma-NETZSCH thermal analyser in the temperature range 35–600 °C with a heating rate of 10 °C per minute under nitrogen gas flow. Absorption spectra in solution and thin films were recorded using a UV-Visible (Agilent Cary 60) spectrophotometer. Steady state emission spectra were recorded using an Edinburgh FLS1000 spectrofluorometer. Time-resolved fluorescence emission decay was obtained using the time-correlated single photon counting (TCSPC) technique with a 450 nm nanosecond LED as the excitation source.

2.3 Synthesis

(*Z*)-5-(4-(Diphenylamino)benzylidene)-2-thioxoimidazolidin-4-one (TPA-2TH). 2-TH (0.23 g, 2 mmol) and TPA (0.55 g, 2 mmol) in glacial acetic acid were added to a 100 mL round bottom flask. To this solution, sodium acetate (0.67 g, 8 mmol)

was added and the reaction mixture was kept for refluxing at 120 °C under a nitrogen atmosphere. The progress of the reaction was monitored using TLC chromatography. After completion of the reaction (24 h), the mixture was poured into ice-cold water. The residue obtained was filtered off to obtain the crude product which was further purified using column chromatography (ethyl acetate/hexane) to obtain an orange coloured solid in 86% yield. Melting point: 250–252 °C. ^{1}H-NMR (500 MHz, DMSO-d_6) δ (ppm): 12.28 (s, 1H), 11.99 (s, 1H), 7.61–7.63 (d, J = 8.3 Hz, 2H), 7.33–7.36 (t, J = 7.4 Hz, 4H), 7.08–7.13 (m, 6H), 6.82–6.86 (d, J = 10.1 Hz, 2H), 6.43 (s, 1H). ^{13}C-NMR (75 MHz, $CDCl_3$ + DMSO-d_6) δ (ppm): 193.79 (–C═S), 165.47 (–C═O), 125.07–151.33 (aromatic carbon), 141.77 (2TH carbon), 116.97 (ethylene carbon); HR-MS: calculated for $C_{22}H_{17}N_3OS$ (m/z): 371.1092; found: 372.1230 $[M + H]^+$.

2.4 Zebrafish studies

To determine the toxic effects of **TPA-2TH** on the development of zebrafish, a range of 10, 20, 40, 60, 80, and 100 μg mL^{-1} concentrations were tested on 4 hpf (hours post fertilized) zebrafish embryos in a 24 well plate by following OECD 236, Fish embryo toxicity test guidelines (OECD236, 2013) for a duration of 96 h, analysed for the % of mortality and % of hatching rate during exposure tenure. In a separate set of experiments, 72 hpf larvae were used to quantify the fluorescence quenching. On day one, larvae were treated with a 10 μg mL^{-1} concentration of **TPA-2TH** along with the control and solvent control. On the next day, 10 μg mL^{-1} $HgCl_2$ and $CuCl_2$ were added to the same plate and kept for incubation. On the third day, the fluorescence images were collected using a Nikon Eclipse Ti2, New York, USA and the fluorescence was quantified using Image J software. Furthermore, the change in fluorescence before and after the addition of $HgCl_2$ and $CuCl_2$ was calculated. To study the effect of **TPA-2TH** on the behaviour, we conducted an acute behavioural toxicity assay by using adult zebrafish. A small glass tank with a dimension of 15 × 12 × 9 cm filled with 1 L of water with a single healthy fish and 10 mg L^{-1} of **TPA-2TH** was used. The concentration was selected based on the same concentration used to study the fluorescence quenching in zebrafish larvae. The experiment was repeated thrice and behavioural end points were recorded.

3. Results and discussion

TPA-2TH was synthesized *via* a one pot Knoevenagel condensation reaction between 2TH and 4-(diphenylamino)benzaldehyde (TPA-CHO) under acidic conditions as described in Scheme 1. The ensuing compound **TPA-2TH** was purified by column chromatography and characterized by FT-IR, ^{1}H and ^{13}C NMR, HR-MS and single-crystal XRD (SC-XRD) studies. The detailed characterization is provided in the ESI† (Fig. S1–S4). The functionality –C═O and –C═S of the 2TH ring was observed at ∼1718 and ∼1645 cm^{-1}, respectively in FT-IR spectra. The peak at ∼3169 cm^{-1} was assigned to –NH of the 2TH unit (Fig. S1, ESI†). Two different –NH protons in the ^{1}H NMR spectrum (Fig. S2, ESI†) of **TPA-2TH** resonated at δ 12.28 and 11.99 ppm due to the different chemical environments around them. The aromatic protons of the TPA moiety appeared in the range δ 6.82–7.63 ppm. The peak at δ 6.41 ppm corresponds to the ethylene proton conjugated between TPA and the 2TH unit. ^{13}C NMR (Fig. S3, ESI†) and HR-MS studies further substantiated the formation of **TPA-2TH**. HR-MS spectra (Fig. S4, ESI†) of **TPA-2TH** showed the molecular ion peak at m/z 372.1230 $[M + H]^+$ along with other fragmented peaks, which are in excellent agreement with the respective formulations.

The structure of **TPA-2TH** was further confirmed by SC-XRD analysis. Plate-shaped orange-yellow coloured crystals were obtained from a solvent mixture of toluene/acetonitrile (3 : 2, v/v) using a slow solvent evaporation technique at ambient temperature[51] (Fig. 1). **TPA-2TH** (CCDC 2278085†) crystallizes in the monoclinic crystal system with a $P2_1/n$ space group and shows a co-facial herringbone molecular arrangement in the crystal lattice. Oxygen, sulphur and –NH groups of **TPA-2TH** are connected by strong dimeric N–H···S and N–H···O hydrogen bonds on either side with bond lengths of 2.424 Å and 1.926 Å, respectively, along with a C–H···O intermolecular interaction distance of 2.575 Å. The molecular arrangement is also stabilized by ethane H···H-aromatic (2.336 Å), C═O···H-aromatic (2.575 Å), N–H···C═O (2.831 Å) and C═S···C-aromatic (3.397 Å) interactions. The π–π interaction distance between the aromatic ring (connected to ethane) and the 2TH ring appears to be 4.765 Å. Furthermore, the intramolecular C–H···π interaction distances among three overcrowded phenyl rings of 3.053 Å, 3.060 Å and 3.148 Å were also observed. The three phenyl rings enabled a more twisted torsional angle of 140.46° among them and a twisted torsional angle of 149.80° between the middle phenyl ring and the 2TH moiety. The detailed crystallographic data are summarized in Table 1. Fig. S5 (ESI†) depicts the Hirshfeld surfaces of **TPA-2TH** mapped across a d_{norm} range of 0.5 to 1.4. The prominent interactions between –NH and –C═O oxygen atoms are shown by the bright red spots on the d_{norm} map. In contrast, the blue patches represent all weaker intermolecular interactions with more considerable distances (Fig. S5a, ESI†). Two prominent sharp spikes in the 2D fingerprint plot represent the O···H intermolecular interaction, while the intermolecular contact involving S···H is indicated by the two brief sideways spikes (Fig. S5b, ESI†). Fig. S5c (ESI†) illustrates the contribution of individual intermolecular interactions based on a 2D fingerprint plot of Hirshfeld analysis which revealed that H···H (42.8%) and C···H (26.1%) intermolecular interactions are primarily responsible for the molecular packing. The contributions of S···H, N···H, and O···H are found to be 12.2, 8.9 and 3.6%, respectively. Additionally, 3.1% of the area accounts for π···π interactions.

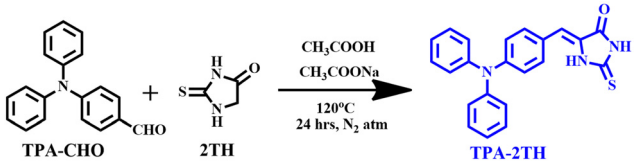

Scheme 1 Synthetic route for **TPA-2TH**.

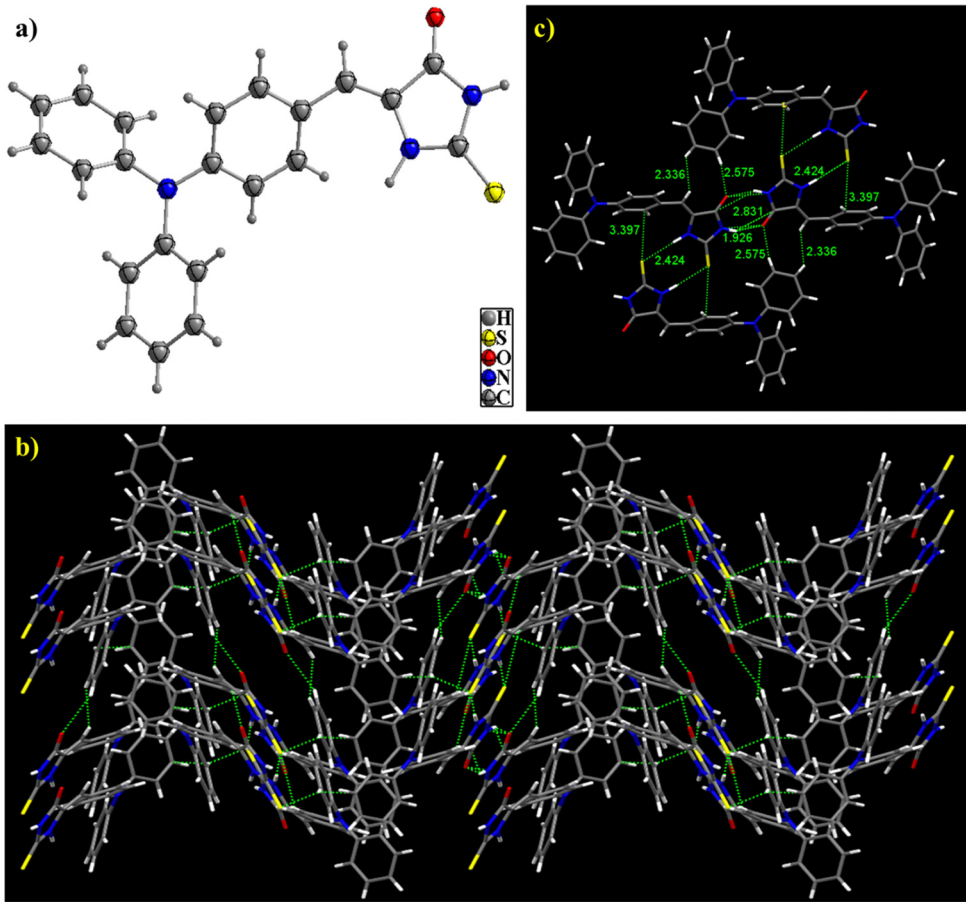

Fig. 1 (a) Single crystal X-ray structure of **TPA-2TH** with 30% of the thermal ellipsoids. (b) Supramolecular arrangement of **TPA-2TH** in a crystal lattice. (c) Depiction of the crystal packing of the dimeric hydrogen bonding with N–H···S, N–H···O and C–H···O hydrogen bonds followed by C–H···π intramolecular interactions.

To examine the thermal characteristics of **TPA-2TH**, differential scanning colorimetric (DSC) and thermal gravimetric analysis (TGA) measurements were performed. The DSC results displayed high thermal stability of **TPA-2TH** up to 355 °C with a melting point at 254 °C (Fig. S6a, ESI†). The decomposition of **TPA-2TH** occurred in two stages, as represented in Fig. S6b (ESI†). The initial weight loss of ∼6% started at 175 °C while a significant decomposition of ∼24% occurred at 323 °C attributed to the decomposition of the 2TH unit.

3.1 Photophysical properties

The photophysical properties of **TPA-2TH** were investigated by UV-Visible and photoluminescence (PL) experiments in solution and solid state methods at room temperature. Fig. 2(a) represents the absorption and emission spectra of **TPA-2TH** in THF. They show an intense absorption band at ∼431 nm and other small absorption bands at ∼217 and ∼299 nm, respectively. The most intense absorption peak at 217 nm corresponds to the TPA core and the weak absorption band at 299 nm is assigned to π → π* transitions. The absorption band at λ_{max} ∼431 nm is ascribed to the efficient charge separated state produced by ICT between the TPA donor part of the molecule and the acceptor end group, *i.e.*, 2TH. However, in the thin film, the absorption spectra exhibited two broad red-shifted peaks at 323 and 460 nm. Upon excitation at 431 nm, **TPA-2TH** showed a strong bluish-green emission in THF at 522 nm, predominantly due to ICT with a quantum yield (Φ_f) of 30%. Interestingly, the solid state emission spectra of **TPA-2TH** showed a red shift of ∼76 nm compared to its emission in THF exhibiting an orange-red emission at ∼598 nm (Fig. 2(b)).

It is very well known that on exciting a fluorophore with a D–A interaction system, ICT takes place.[52] Thus, to clearly investigate ICT, the solvatochromic effect of **TPA-2TH** was studied in different organic solvents of varying polarities, since the fluorescence derived from ICT depends intensely on the polarities of solvents. The absorption spectra of **TPA-2TH** in different solvents did not show any significant changes in λ_{max} (430 nm in THF to 436 nm in methanol). A slight positive solvatochromism was observed in the absorption spectra (Fig. S7, ESI†). λ_{max} showed a red shift in polar solvents in comparison to non-polar solvents. This observation reveals that the electronic excitation increases the molecule's dipole moment and the directions of the ground and excited state dipoles are similar.[53,54]

Unlike the absorption spectrum with a negligible effect (Fig. S7a, ESI†), varying solvent polarities exerted a dramatic

Table 1 Summary of the crystallographic data

Compound identification code	**TPA-2TH**
CCDC no.	2278085
Formula	$C_{22}H_{17}N_3OS$
Formula weight	371.44
Temperature (K)	100.00(10)
Crystal system	Monoclinic
Space group	$P2_1/n$
a (Å)	9.4332(7)
b (Å)	20.7152(16)
c (Å)	9.7429(7)
α (°)	90.00
β (°)	109.03(8)
γ (°)	90.00
Volume (Å^3)	1799.8(2)
Z	4
Density, ρ_{calc} (g cm$-^3$)	1.371
Abs. coeff., μ (mm^{-1})	0.197
F (000)	776
2θ range for data collection (°)	3.269 to 24.998
Crystal size (mm$_3$)	0.25× 0.18 × 0.12
Radiation	MoKα (λ = 0.71073)
Index ranges	$-11 \leq h \leq 11$, $-24 \leq k \leq 24$, $-11 \leq l \leq 11$
Reflections collected	20 673
Independent reflections	2452 [R_{int} = 0.1208, R_{Sigma} = 0.0971]
Data/restraints/parameters	2452/0/244
Goodness-of-fir on F^2	1089
Final R indexes [$I \geq 2\sigma(I)$]	R_1 = 0.0673, wR_2 = 0.1104
Final R indexes [all data]	R_1 = 0.1023, wR_2 = 0.1241

influence on the emission of **TPA-2TH** as depicted in Fig. 3. On increasing the solvent polarity, a significant red shift in emission maxima (λ_{em}) was observed. λ_{em} of **TPA-2TH** in trimethylamine is 492 nm, whereas it is 573 nm in acetonitrile. On increasing the polarity from trimethylamine to acetonitrile, a bathochromic shift of ~81 nm was observed. Based on these results, it was concluded that the effect of solvent polarities is more pronounced on λ_{em} than on λ_{abs}, suggesting that the molecule's excited state is controlled by dipole–dipole interactions and the dipole moments of excited states are higher than those of the ground states.[55,56] Additionally, this insignificant change in absorption maxima and a considerable variation in fluorescence emission (λ_{em}) indicate the formation of a twisted ICT (TICT) transition.[57] Furthermore, the difference in the full-width half-maximum or width of the peak confirms that polar solvent molecules stabilize the emission and the excited states giving wider spectra.[58] This broad emission pattern of **TPA-2TH** due to the polar solvent proves the existence of the ICT transition between donor TPA to acceptor 2TH.

Furthermore, to comprehend the solvent polarity influence of **TPA-2TH** in different solvents, a Lippert–Mataga plot was used, which shows that the Stokes shift ($\Delta\bar{\nu}$) of the compound is solvent dependent and is governed by the change in the dipole moment of the molecule upon excitation, refractive index (η) and the dielectric constant (ε) of the solvent used.[59] Fig. 3b and Table S1 (ESI†) depict the Lippert–Mataga plot and its parameter for **TPA-2TH** in different solvents. The plot shows that two types of linearity, one for polar protic solvents like AcOH and MeOH and the other for polar aprotic solvents such as hexane, toluene, CCl_4, DCM, $CHCl_3$, EtOAc, *etc.* In aprotic solvents, **TPA-2TH** exhibited a general solvent effect; however, in MeOH and ACOH, it deviated from the linearity due to specific interactions, such as H-bonding.

With increasing solvent polarity, the Stoke's shift increases, but the fluorescence quantum yields were found to be decreased. This is caused by increased solvent polarity, which facilitates the non-radiative deactivation of the fluorescent state of the molecule. Table S1, ESI,† shows the results of the fluorescence quantum yield measurement of **TPA-2TH** at room temperature with various solvent polarities and hydrogen bonding capacities. In low polarity solvents, TPA showed a high quantum yield, but in highly polar solvents, it showed a relatively poor quantum yield. To identify the different species present in the excited state, the fluorescence lifetime of **TPA-2TH** in various solvents was measured (Fig. S8, ESI†). Table S1, ESI,† represents the time-resolved data in terms of average lifetime (τ_{avg}), regardless of the solvent polarity, for all solvent profiles that are well fitted into mono and bi-exponential decay. The lifetime decay processes of TPA are discovered to be solvent dependent. The fluorescence lifetime was shown to decrease with an increase in solvent polarity. For instance, the lifetime in CCl_4 is 3.56 ns, but AcOH, a polar solvent, shortened it to 1.14 ns.

Furthermore, the pH-dependent properties of **TPA-2TH** were investigated by recording its absorption and emission spectra in an aqueous medium covering a pH range from 1 to 14

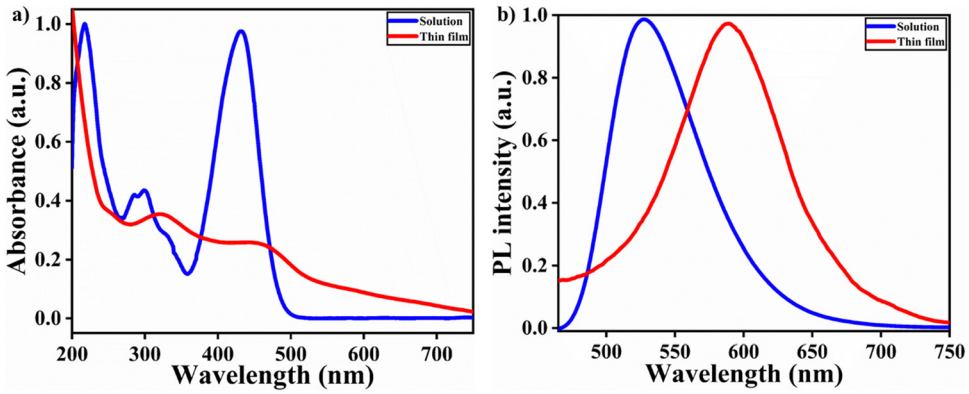

Fig. 2 Absorption (a) and emission spectra (b) of **TPA-2TH** in solution and in a thin film.

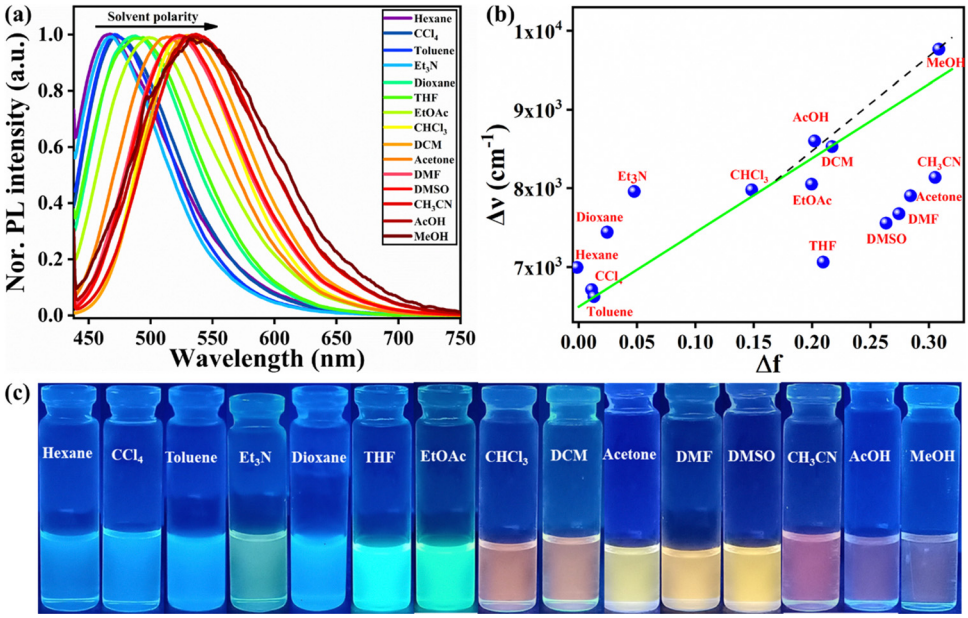

Fig. 3 (a) Emission spectra of **TPA-2TH** (λ_{ex} = 431 nm) in different solvents, (b) Lippert–Mataga plot in different solvents showing the dependence of the Stokes shift ($\Delta\bar{\nu}$) of **TPA-2TH** on the solvent polarity function Δf and (c) photographs showing the changes in emission of **TPA-2TH** in different solvents under the illumination of UV light (365 nm).

(Fig. S7b and c, ESI†). The pH adjustments were achieved using diluted HCl for acidic conditions and NaOH for basic conditions. The initial weak intensity of the 265 nm peak in the absorption spectra at pH = 1 suggests a suppressed $\pi \rightarrow \pi^*$ transition, likely due to acidic conditions affecting the electronic structure. As the pH was increased to 10, the increased intensity of the 265 nm peak indicates a more pronounced $\pi \rightarrow \pi^*$ transition, possibly due to reduced protonation effects on the molecule. The subsequent decrease in intensity of the 265 nm peak as the pH increased from 10 to 14 may be attributed to deprotonation events impacting the molecular conformation or electronic interactions, leading to altered UV absorption properties. Furthermore, a weak yet intense ICT peak was evident at 478 nm at a pH less than 10. Intriguingly, this ICT peak underwent a blue shift, shifting to 430 nm on increasing the pH from 10 to 14 (Fig. S7b, ESI†). The blue shift of the ICT peak from 478 nm to 430 nm with increasing pH further indicates a change in charge distribution or electronic transitions within **TPA-2TH** molecules under basic conditions. In the PL spectra (Fig. S7c, ESI†), a notable blue shift in emission maxima was observed at higher or basic pH levels compared to its emission under acidic conditions. This intriguing shift in emission maxima, concomitant with varying pH levels, indicates that the electronic structure and intermolecular interactions within **TPA-2TH** are markedly influenced by the pH of the solution.

3.2 Sensing response of TPA-2TH with various metal ions

Since the functional groups of **TPA-2TH** are electron-donating, we hypothesized that this might translate to a greater affinity for metal ions. Thus, the fine-tuning of **TPA-2TH** fluorescence prompted us to investigate its sensitivity and selectivity to specific metal ions. Bearing in mind the flexible coordination of N, S and O atoms and to evaluate the potential of **TPA-2TH** as a fluorescent sensor for the detection of metal ions, fluorescent titrations were performed.

The sensing competence of **TPA-2TH** towards different metal ions like Ba^{2+}, Mg^{2+}, Mn^{2+}, Co^{2+}, Ni^{2+}, Cu^{2+}, Zn^{2+}, Pb^{2+}, Pd^{2+}, As^{2+}, Cd^{2+} and Hg^{2+} was studied by taking 1 mM stock solution of both **TPA-2TH** in THF and each metal ion in their salt forms (chloride, acetate and nitrate salts) in methanol (Fig. 4(a)). Remarkably, among all metal ions, only Hg^{2+} showed the fluorescence quenching of **TPA-2TH** with a concomitant blue shift (from 522 to 502 nm) and the appearance of a new peak at 643 nm (Fig. 5(c)). In contrast, all other metal ions displayed a relatively less or negligible change in emission intensity of **TPA-2TH**. From Fig. 4(b), it is clear that **TPA-2TH** binds selectively only to the Hg^{2+} over other metal ions.

3.3 Selectivity of TPA-2TH towards metal ions

Furthermore, to understand the selective binding of **TPA-2TH** to Hg^{2+} over other metal ions, systematic fluorescence emission titration experiments were performed. It was observed that the emission spectrum of **TPA-2TH** underwent significant variations with an increase in the concentrations of Hg^{2+} ions (0–6.7 μM). The emission peak at 522 nm was gradually decreased and reached the saturation at 6.7 μM of Hg^{2+} (Fig. 5(b)) along with the formation of a new peak at 643 nm. The huge fluorescence quenching can be ascribed to the heavy atom effect of Hg^{2+} ions upon binding with the fluorophore.[32] To look further into the complex formation between **TPA-2TH** and Hg^{2+} ions, UV-Vis titration was carried out in THF (Fig. 5(a)). Upon the addition of different concentrations of Hg^{2+}, the ICT

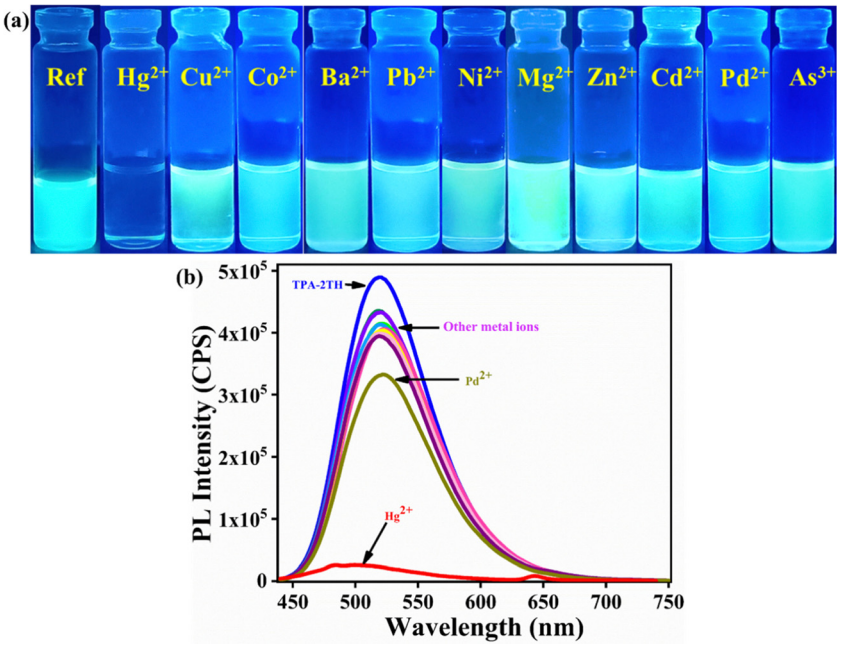

Fig. 4 (a) Photographs of **TPA-2TH** in the presence of different metal solutions under the UV light of 365 nm. (b) Emission spectra of **TPA-2TH** (3 μM) in the absence and presence of different metal ions (6.7 μM) in THF.

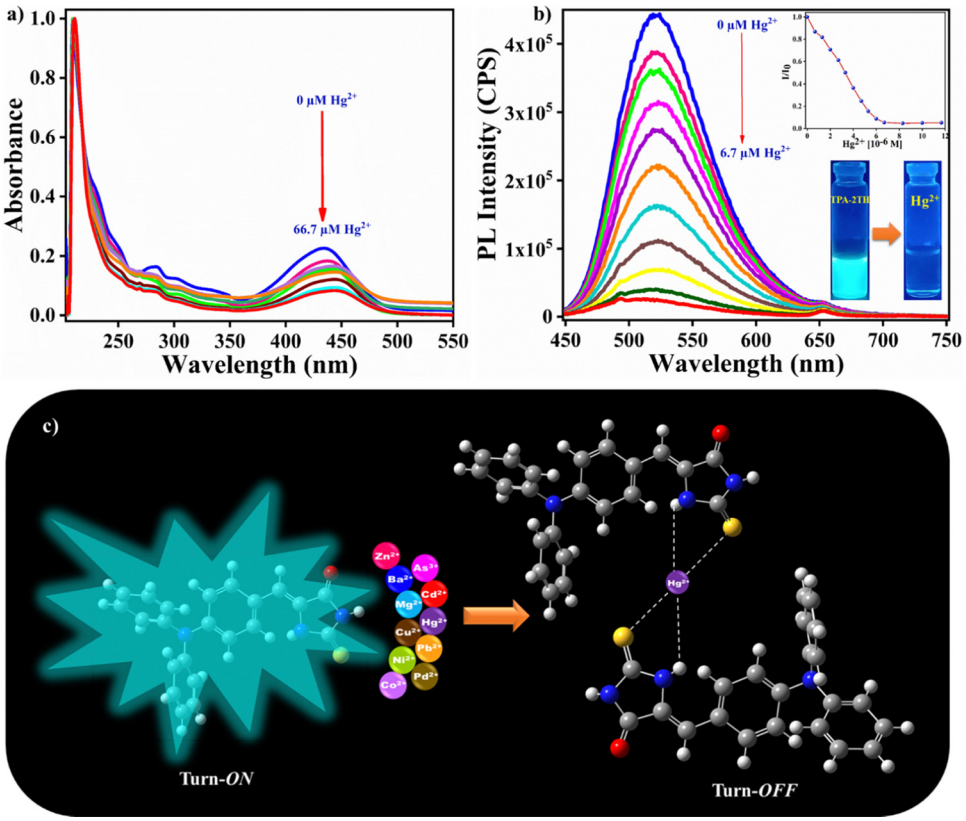

Fig. 5 Change in (a) absorbance and (b) emission spectra of **TPA-2TH** (3 μM) upon the addition of different concentrations of Hg^{2+} in THF. The inset shows the changes in I/I_0 of **TPA-2TH** (3 μM) with increasing concentrations of Hg^{2+} (0–6.7 μM). (c) Pictorial representation of Hg^{2+} sensing by **TPA-2TH**.

band of **TPA-2TH** appearing at 431 nm gradually moved with a bathochromic shift to 444 nm. These results further support the decrease in the emission intensity of **TPA-2TH** upon the addition of Hg^{2+} ions. Many heavy transition metal (HTM) ions are well-

known fluorescence quenchers due to their paramagnetic properties and the heavy atom effect.[60]

For practical quantitative detection, the fluorescence intensity changes should vary linearly with the analyte. To examine the sensitivity of **TPA-2TH** towards Hg^{2+} ions, the limit of detection (LOD) was calculated by performing fluorescence titration of **TPA-2TH** (0.067 μM) in THF (Fig. S9, ESI†), following the procedure recommended by IUPAC[61] which involved plotting the emission intensity of the probe against increasing concentrations of Hg^{2+}. The linear response of the fluorescence intensity of **TPA-2TH** as a function of increasing Hg^{2+} concentration was observed from 17 nM to 67 nM (R^2 = 0.9826). The LOD was calculated to be 3.3 pM, which was well below the permissible limit of Hg^{2+} in drinking water (2 ppb) set by the US Environmental Protection Agency.[62,63] These results indicate that **TPA-2TH** can be used to detect the picomolar concentration of Hg^{2+} ions and is found to be highly sensitive to other reported sensory probes for Hg^{2+} detection (Table S2, ESI†). A characteristic feature of any sensory probe is its high selectivity towards a particular analyte over other interfering competitive species. The spectral response of probe **TPA-2TH** towards other metal ions (Ba^{2+}, Mg^{2+}, Mn^{2+}, Co^{2+}, Ni^{2+}, Cu^{2+}, Zn^{2+}, Pb^{2+}, Pd^{2+}, As^{3+}, and Cd^{2+}) besides Hg^{2+} was tested in THF. The change in fluorescence intensity of **TPA-2TH** (3 μM) was measured by adding 1 equivalent of other metal ions (Fig. 6(a)).

The influence on the fluorescence intensity of **TPA-2TH** due to other metal ions was found to be negligible even at the micro-molar level. In contrast, the highly selective fluorescence quenching by Hg^{2+} ions was observed for **TPA-2TH** with a quenching efficiency of 94.4% at 522 nm. This excellent selectivity of the probe **TPA-2TH** in the presence of other competitive metal ions was mainly due to the stronger affinity of the thio groups of 2TH to Hg^{2+}. Thus, Hg^{2+} ions being more thiophilic bind with **TPA-2TH** selectively even in the presence of a high concentration of the other metal ions. These results emphasize that **TPA-2TH** can be used exclusively as a highly sensitive sensor for Hg^{2+} ion detection. A fluorescence-based Job's experiment was performed to study the complexation between **TPA-2TH** and Hg^{2+} ions (λ_{ex} = 430 nm, λ_{em} = 522 nm). As shown in Fig. 6(b), the plot of fluorescence intensity *versus* mole fraction of **TPA-2TH** displays a point of intersection corresponding to two linear extrapolations, which is found to be the 0.6 mole fraction of **TPA-2TH**, indicating 2 : 1 complex formation between **TPA-2TH** and Hg^{2+} ions.

3.4 ^{1}HNMR titration of TPA-2TH with Hg^{2+} ions

To further understand the nature of the interaction between **TPA-2TH** and Hg^{2+} ions, the ^{1}H NMR titration experiment in DMSO-d_6 (Fig. 7) was performed. It was found that two singlets due to two –NH protons were merged and broadened with a downfield shift, thus appearing at δ 12.27 ppm and its intensity decreased gradually upon increasing the Hg^{2+} concentration from 0 to 0.25 to 1.5 equivalents. The protons of the region from δ 6.89–7.65 ppm increased and became twice the number of original values indicating 2 : 1 (**TPA-2TH** + Hg^{2+}) complex formation between Hg^{2+} and **TPA-2TH** through its –NH and S atom owing to the soft–soft interaction between S and Hg^{2+}.

3.5 Mechanistic studies

The results from steady-state fluorescence measurements using a Stern–Volmer plot (SV) and time-resolved studies are used to investigate the quenching mechanism of sensing, providing a deeper understanding of the process.[64–66] The fluorescence quenching upon titration between **TPA-2TH** and Hg^{2+} ions indicates strong binding interactions between them. The SV plot demonstrates a direct relationship between the change in emission and the concentration of Hg^{2+} ions at low concentrations (up to 1.5 μM). The quenching constant K_{SV} was obtained from the SV equation as follows:

$$\frac{I_0}{I} = 1 + K_{SV}[Q]$$

where I_0 and I is the fluorescence intensity of **TPA-2TH** in the absence and presence of Hg^{2+} ions, respectively, K_{SV} is the Stern–Volmer quenching constant and [Q] is the concentration of Hg^{2+} ions. The Stern–Volmer plot of I_0/I *vs.* [Q] was plotted to obtain the slope value as K_{SV} (Fig. 8(a)). The linear relationship observed at lower concentrations (K_{SV} = 2.02 × 10^6 M^{-1}) can be

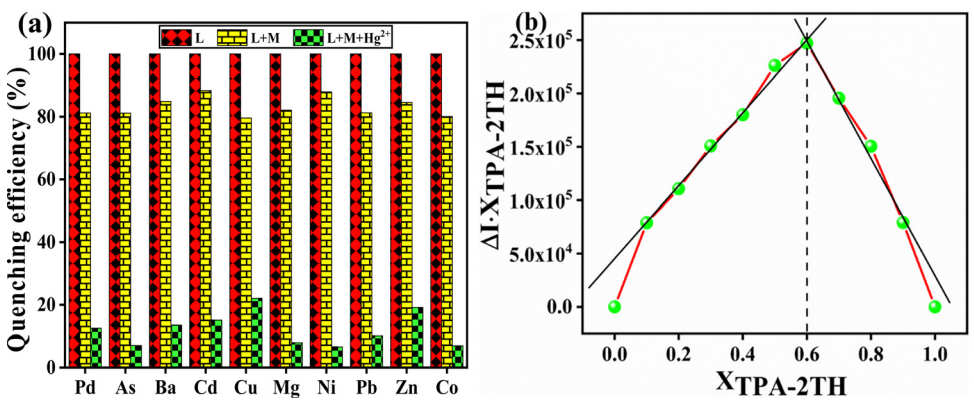

Fig. 6 (a) Interference effect of various metal ions on the emission intensity of **TPA-2TH** at 522 nm in THF. (b) Job's plot for complex formation between **TPA-2TH** and Hg^{2+} in THF/H_2O (λ_{ex} = 430 nm).

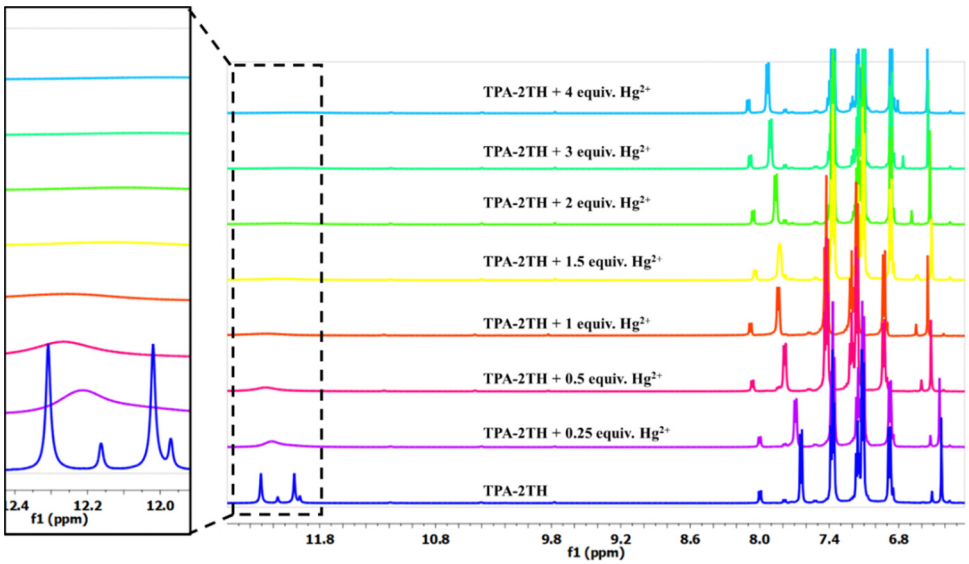

Fig. 7 Partial ^{1}HNMR spectra of **TPA-2TH** upon the addition of different concentrations of Hg^{2+} as $HgCl_2$ in DMSO-d_6.

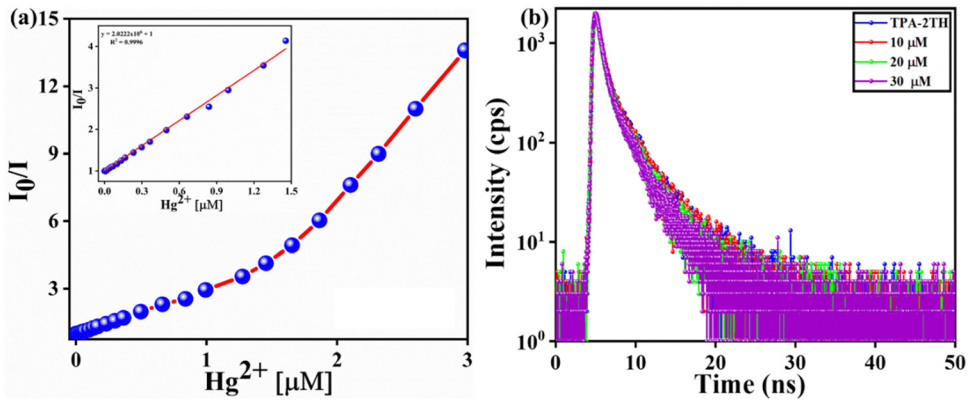

Fig. 8 (a) SV plot and (b) time-resolved fluorescence emission decay of **TPA-2TH** and the **TPA-2TH** + Hg^{2+} complex in THF.

attributed to either static or dynamic quenching mechanisms. However, at higher concentrations, there is a deviation from linearity, suggesting the involvement of static quenching with the contribution of dynamic quenching. Based on these findings, we propose the co-existence of both static and dynamic quenching mechanisms. The relatively gradual curvature indicates the dominance of the static quenching mechanism, indicating the formation of a ground state complex between the fluorophore **TPA-2TH** and Hg^{2+} ions.[66] Fluorescence lifetime investigation is the best technique to determine the quenching mechanism, as the static fluorescence quenching does not affect the lifetime, whereas dynamic quenching shows variations in the lifetime as a function of concentration and its environment. Lifetime studies were carried out to demonstrate the coordination between **TPA-2TH** and Hg^{2+} and to establish the quenching fluorescence mechanism. The decay profiles were determined in THF and then fitted with bi-exponential functions. The average fluorescence decay ($\tau_{aver.}$) of 30 μM of the **TPA-2TH** + Hg^{2+} complex was 3.08 ns (Fig. 8(b)), which is almost similar to that of **TPA-2TH** ($\tau_{aver.}$ = 3.13 ns), suggesting that static quenching is the predominant mechanism. Normally, the formation of a ground state complex does not cause a significant red shift in the absorption spectrum of the fluorophore.[64] However, in the presence of Hg^{2+} ions, a slight bathochromic shift of ~13 nm was observed in the absorption spectrum of the **TPA-2TH** probe (Fig. 5(a)). This shift provides additional evidence for the formation of a ground state complex and further confirms the predominance of the static quenching mechanism.

To further understand the quenching mechanism, we have calculated the radiative and non-radiative rate constants for **TPA-2TH** and its Hg^{2+} complex based on their quantum yield (Φ_f) and average lifetimes ($\tau_{aver.}$).[67,68] Table S3, ESI,† provides an insight into the decay components contributing to the quenching mechanism. A higher k_r signifies efficient light emission, with **TPA-2TH** displaying 0.096 ns^{-1} k_r while **TPA-2TH** + Hg^{2+} exhibits an exceptionally low k_r value of 0.001 ns^{-1}, indicating inefficient light emission. On the other hand, k_{nr} denotes the rate of non-emissive decay pathways.

TPA-2TH has a k_{nr} of 0.224 ns^{-1}, suggesting a significant non-emissive contribution, whereas **TPA-2TH** + Hg^{2+} has a notably higher k_{nr} value of 0.324 ns^{-1}, indicating a dominant non-radiative decay route.

The following equation can be used to calculate the fractional occupancy of all binding sites (θ)[69] present in **TPA-2TH:**

$$\theta = \frac{\Delta I}{\Delta I_{max}} = \frac{I - I_0}{I_{max} - I_0}$$

where ΔI_{max} is the maximal fluorescence change seen when all of the acceptor binding sites are occupied by the ligand. Thus, the association constant K_a can be obtained using the following formula:[70]

$$\frac{1}{(1-\theta)K_a} = \frac{[Hg^{2+}]}{\theta} - n[\text{TPA-2TH}]$$

where n denotes the total number of binding sites, θ denotes the amount of Hg^{2+} ions that bind to the probe **TPA-2TH** and K_a means the association constant. The plot of $1/(1-\theta)$ *vs.* $[Hg^{2+}]/\theta$ will give K_a as the slope value, which is obtained as 1.6×10^6 M^{-1} (Fig. S10, ESI†). The standard free energy change[69] can be calculated using the equation $\Delta G = -2.303RT \log_{10} K_a$, which was found to be −35.59 kJ. The negative value for ΔG indicates that the complexation reaction between **TPA-2TH** and Hg^{2+} ion is spontaneous.

Furthermore, the binding mode of **TPA-2TH** towards Hg^{2+} and the associated quenching mechanisms could be explained based on soft–soft metal interactions between Hg^{2+} and S and NH atoms **TPA-2TH**. Upon binding of Hg^{2+} with **TPA-2TH**, there is an overall reduction in the electron density from the donor TPA moiety to the acceptor 2TH, which led to quenching in the fluorescence emission of **TPA-2TH**. Furthermore, **TPA-2TH** exhibited reversible sensing capabilities for Hg^{2+}. Notably, the addition of potassium iodide was able to effectively reverse the sensing event. This reversal can be attributed to the stronger affinity of Hg^{2+} for iodide ions. The switching phenomenon could be achieved through multiple cycles of alternating additions of Hg^{2+} and KI ions to the **TPA-2TH** solution (Fig. S11, ESI†).

To explore the time-dependent properties, the emission spectra of **TPA-2TH** were acquired in THF by adding a 3 μM solution of Hg^{2+}. The emission peak intensity was monitored at 522 nm over varying time intervals (Fig. S12, ESI†). After adding Hg^{2+} to **TPA-2TH** solution at 84 s, a notable reduction in emission intensity at 522 nm was observed. Interestingly, beyond 84 s, the emission intensity reached a point of saturation. Even when extending the time to 280 s, no further change in emission intensity at 522 nm was observed. The observed time-dependent decrease in emission intensity until reaching a saturation point at 84 s can be attributed to a specific interaction or dynamic process involving Hg^{2+} ions and **TPA-2TH**. The saturation of emission intensity beyond 84 s suggests that the interaction between **TPA-2TH** and Hg^{2+} ions stabilizes or reaches a state of equilibrium at this time point. Further temporal extension does not significantly influence this interaction, indicating a steady-state condition in the emission behaviour of **TPA-2TH**.

3.6 Fluorescence quenching studies in zebrafish larvae

Utilizing the zebrafish in multiple research areas, such as cancer, drug discovery, toxicology, developmental biology, neuroscience, and infectious disease modelling[71,72] has proven to be a valuable model organism due to its low cost of maintenance, high fecundity, and the ease with which its genome can be manipulated and observed.[73] A lot of studies have been carried out to evaluate the toxicity of chemical substances, pollutants, environmental contaminants, and drugs, based on teratological, biochemical, and behavioural analyses. However, there is lack of studies on live animal models to test the fluorescence quenching as a bio-indicator. We tried to address the fluorescence quenching as a bio-indicator for metal ion

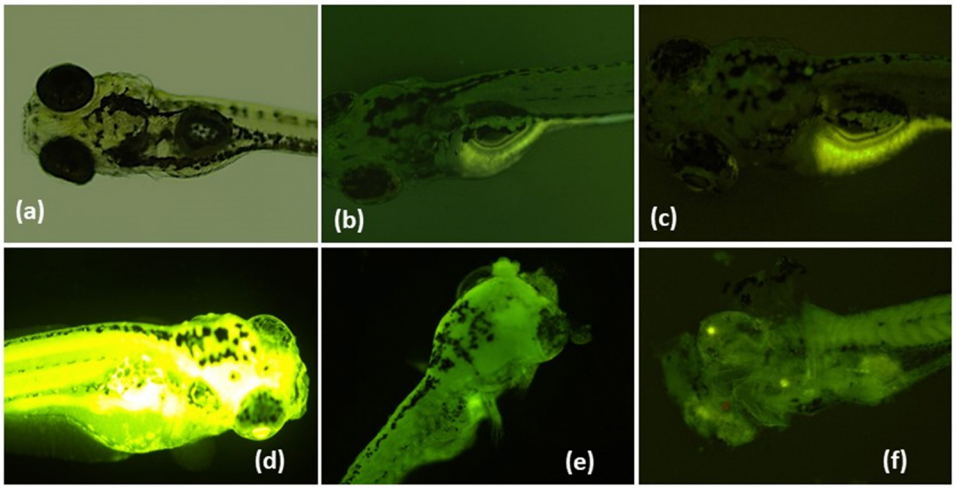

Fig. 9 Quantification of fluorescence quenching in live zebrafish larvae. Images showing different intensities of fluorescence emission. (a) Bright field image of zebrafish larva. (b) Zebrafish larva treated with water. (c) Larva treated with DMSO. (d) **TPA-2TH** treated larva showing a high intensity of fluorescence emission. (e) Larva treated with **TPA-2TH** + $CuCl_2$. (f) **TPA-2TH** + $HgCl_2$ treated zebrafish larva.

contamination using zebrafish larvae as a model system along with acute behavioural toxicity end points using adult zebrafish.

The strong fluorescence emission was observed in zebrafish larvae of 72 hpf when treated with **TPA-2TH** (Fig. 9). Compared to zebrafish larvae treated with **TPA-2TH** alone, the intensity of fluorescence was reduced in **TPA-2TH** + $HgCl_2$ by 61.11% and in **TPA-2TH** + $CuCl_2$ by 80.37%. The fluorescence intensity among water control and DMSO control treated larvae were found to be equal. Moreover, during the course of treatment the zebrafish larvae were found to be dead because of the toxicity of $CuCl_2$ and $HgCl_2$. The pristine **TPA-2TH** is safe to use for zebrafish larvae but with the combination of Hg^{2+} and Cu^{2+}, it was found to be detrimental.

3.7.1 Zebrafish hatching studies. The hatching rate of embryos treated with **TPA-2TH** was 100% at lower concentrations like 10, 20, and 40 μg mL^{-1} tested which is equitant to the control and solvent control hatching percentage. However, no further hatching and larvae also died with concentrations 60, 80 and 100 μg mL^{-1}. This might be due to the highly viscous nature of the compound at higher concentrations, which made a delay in hatching, ultimately leading to the death of zebrafish larvae.

3.7.2 Acute behavioural toxicity. Acute behavioural toxicity analysis of zebrafish exposed to **TPA-2TH** revealed that the compound did not at all cause any behavioural abnormalities. Behavioural end points like sound response, fear response, mirror biting, bottom dwelling and surface moving are all found to be alike those of the controls (Fig. S13, ESI†).

4. Conclusions

In this work, we have designed and developed a novel triphenylamine (TPA) appended in conjugation with 2TH through a one pot Knovenagel condensation method with good yields and its structure was confirmed using FT-IR, NMR, HR-MS and SC-XRD techniques. In the molecular ensemble, the TPA moiety acted as a donor and the **2TH** unit acted as an Hg^{2+} ion chelator. SC-XRD revealed the co-facial herringbone packing arrangement of **TPA-2TH** in a crystal lattice with a propeller-shaped TPA unit. It exhibited a strong absorption band at 431 nm and showed strong yellow-green emission in THF with λ_{em} = 522 nm that is attributed to the efficient charge-separated state produced by ICT between the TPA and 2TH unit. **TPA-2TH** showed an excellent solvatochromic effect wherein it exhibited a bathochromic shift in its emission on increasing the solvent polarity. **TPA-2TH** exhibited distinct fluorescence quenching upon complexation with Hg^{2+} ions, attributed to increased spin–orbit coupling and a weakened ICT effect. The LOD achieved was as low as 3.3 pM, indicating the high sensitivity of **TPA-2TH** for Hg^{2+} ion detection. The fluorescence quenching of **TPA-2TH** in zebrafish larvae provided a sensitive indicator for metal ion contamination, while the absence of acute behavioural toxicity in adult zebrafish suggested its safety for aquatic organisms. This study highlights the practical utility of **TPA-2TH** as a comprehensive tool for evaluating metal ion contamination and assessing its potential toxic effects on aquatic ecosystems. Further research can explore its efficacy in detecting and quantifying diverse pollutants or contaminants in environmental samples. Moreover, **TPA-2TH** shows promise for evaluating the presence and toxicological impacts of various substances on different organisms and aquatic ecosystems.

Author contributions

Pratiksha Gawas: conceptualization, methodology, investigation, formal analysis, visualization and writing – original draft. Dr Buthanapalli Ramakrishna: crystallography. Dr Rajesh Pamanji and Dr Joseph Selvin: performed experiments related to Zebrafish studies. Dr Venkatramaiah Nutalapati: conceptualization, review, editing, funding acquisition and supervision.

Conflicts of interest

The authors declare no competing financial interest.

Acknowledgements

The authors acknowledge the financial support from SRMIST for this research work and the various in-campus characterization facilities at NRC, SCIF of SRMIST. Dr NVR greatly acknowledges the Central Power Research Institute (CPRI, A government of India society under Ministry of Power) for funding through the R&D project (CPRI/R&D/TC/GDEC/2022) and SRMIST for the seed grant. PG thanks SRMIST for the PhD fellowship. The authors are also very thankful to Dr S. Ravi Teja, SSCU, Indian Institute of Science (IISc), Bangalore for the useful discussions. Dr Rajesh Pamanji is thankful to University Grant Commission (UGC), Govt. of India, for providing financial assistance in the form of Dr DS Kothari Postdoctoral fellowship BL/19-20/0302.

References

1 D. F. Perepichka and M. R. Bryce, *Angew. Chem., Int. Ed.*, 2005, **44**, 5370–5373.
2 J. Y. Lee, K. S. Kim and B. J. Mhin, *J. Chem. Phys.*, 2001, **115**, 9484–9489.
3 F. Bureš, O. Pytela, M. Kivala and F. Diederich, *J. Phys. Org. Chem.*, 2011, **24**, 274–281.
4 H. A. M. Van Mullekom, J. A. J. M. Vekemans, E. E. Havinga and E. W. Meijer, *Mater. Sci. Eng., R*, 2001, **32**, 1–40.
5 B. J. Coe, *Chem. – Eur. J.*, 1999, **5**, 2464–2471.
6 P. Lasitha and E. Prasad, *RSC Adv.*, 2015, **5**, 41420–41427.
7 C. Agarwal and E. Prasad, *RSC Adv.*, 2014, **4**, 8015–8022.
8 P. Rajamalli and E. Prasad, *Soft Matter*, 2012, **8**, 8896–8903.
9 P. A. Sullivan and L. R. Dalton, *Acc. Chem. Res.*, 2010, **43**, 10–18.
10 F. Chen, J. Zhang and X. Wan, *Chem. – Eur. J.*, 2012, **18**, 4558–4567.

11 F. M. Raymo and M. Tomasulo, *Chem. – Eur. J.*, 2006, **12**, 3186–3193.
12 J. Xue, B. P. Rand, S. Uchida and S. R. Forrest, *J. Appl. Phys.*, 2005, **98**, 124903.
13 X. Zhang, T. T. Steckler, R. R. Dasari, S. Ohira, W. J. Potscavage, S. P. Tiwari, S. Coppée, S. Ellinger, S. Barlow, J. L. Brédas, B. Kippelen, J. R. Reynolds and S. R. Marder, *J. Mater. Chem.*, 2010, **20**, 123–134.
14 J. Kulhánek, F. Bureš, A. Wojciechowski, M. Makowska-Janusik, E. Gondek and I. V. Kityk, *J. Phys. Chem. A*, 2010, **114**, 9440–9446.
15 A. E. Stiegman, E. Graham, K. J. Perry, L. R. Khundkar, L.-T. Cheng and J. W. Perry, *J. Am. Chem. Soc.*, 1991, **113**(20), 7658–7666.
16 C. Dehu, F. Meyers and J. L. Brédas, *J. Am. Chem. Soc.*, 1993, **115**, 6198–6206.
17 J. Huang, W. Wen, Y. Sun, P. Chou and J. Fang, *J. Org. Chem.*, 2005, **70**, 5827–5832.
18 D. Ray, E. Siva, S. Iyer, K. Sadhu and P. K. Bharadwaj, *Dalton Trans.*, 2009, 5683–5687.
19 S. Sivaramapanicker, K. P. Divya, P. Jayamurthy, J. Mathew, V. N. Anupama, D. Susan Philips and P. Anees, *Photochem. Photobiol. Sci.*, 2012, **11**, 1715–1723.
20 C. A. S. P. P. Thilagar, *Inorg. Chem.*, 2014, **53**, 2776–2786.
21 Y. Yan, Y. Zhang and H. Xu, *ChemPlusChem*, 2013, **78**, 628–631.
22 J. Karthikeyan, P. Parameshwara and A. N. Shetty, *Indian J. Chem. Technol.*, 2008, **15**, 493–496.
23 A. Hemamalini, S. K. Mudedla, V. Subramanian and T. Mohan Das, *New J. Chem.*, 2015, **39**, 3777–3784.
24 Y. Li, F. Wei, Y. Lu, S. He, L. Zhao and X. Zeng, *Dyes Pigm.*, 2013, **96**, 424–429.
25 E. Taboada, G. Cabrera and G. Cárdenas, *Bol. Soc. Chil. Quim.*, 2003, **48**, 7–12.
26 T. B. Wei, G. Y. Gao, W. J. Qu, B. B. Shi, Q. Lin, H. Yao and Y. M. Zhang, *Sens. Actuators, B*, 2014, **199**, 142–147.
27 M. Kumar, R. Kumar and V. Bhalla, *Org. Biomol. Chem.*, 2011, **9**, 8237–8245.
28 W. J. Qu, G. Y. Gao, B. B. Shi, T. B. Wei, Y. M. Zhang, Q. Lin and H. Yao, *A highly selective and sensitive fluorescent chemosensor for mercury ions based on the mechanism of supramolecular self-assembly*, Elsevier B.V., 2014, vol. 204.
29 H. F. Wang and S. P. Wu, *Tetrahedron*, 2013, **69**, 1965–1969.
30 P. Thirupathi and K. H. Lee, *Bioorg. Med. Chem.*, 2013, **21**, 7964–7970.
31 Q. Li, M. Peng, H. Li, C. Zhong, L. Zhang, X. Cheng, X. Peng, Q. Wang, J. Qin and Z. Li, *Org. Lett.*, 2012, **14**, 2094–2097.
32 B. K. Rani and S. A. John, *J. Hazard. Mater.*, 2018, **343**, 98–106.
33 C. Zhou, Y. Song and Y. Li, *RSC Adv.*, 2014, **4**, 33614–33618.
34 H. Dai, F. Liu, Q. Gao, T. Fu and X. Kou, *Luminescence*, 2011, **26**, 523–530.
35 C. Chen, H. Dong, Y. Chen, L. Guo, Z. Wang, J. J. Sun and N. Fu, *Org. Biomol. Chem.*, 2011, **9**, 8195–8201.
36 T. Zhang, G. She, X. Qi and L. Mu, *Tetrahedron*, 2013, **69**, 7102–7106.
37 L. Chen, L. Yang, H. Li, Y. Gao, D. Deng, Y. Wu and L. J. Ma, *Inorg. Chem.*, 2011, **50**, 10028–10032.
38 J. Liu, Q. Lin, Y. M. Zhang and T. B. Wei, *Sens. Actuators, B*, 2014, **196**, 619–623.
39 J. Liu, M. Yu, X. C. Wang and Z. Zhang, *Spectrochim. Acta, Part A*, 2012, **93**, 245–249.
40 C. Y. Li, F. Xu, Y. F. Li, K. Zhou and Y. Zhou, *Anal. Chim. Acta*, 2012, **717**, 122–126.
41 J. Choi, S. K. Lee, J. Bae and S. K. Chang, *Tetrahedron Lett.*, 2014, **55**, 5294–5297.
42 G. S. Ravi Kumara, A. Pandith and Y. J. Seo, *Analyst*, 2020, **145**, 4777–4781.
43 V. T. Nguyen, A. Pandith and Y. J. Seo, *Chem. Commun.*, 2020, **56**, 3199–3202.
44 Y. Pandith, A. Luo, Y. Jang, Y. Bae and J. Kim, *Angew. Chem., Int. Ed.*, 2023, **62**, e202215049.
45 P. P. Gawas, B. Ramakrishna, N. Veeraiah and V. Nutalapati, *J. Mater. Chem. C*, 2021, **9**, 16341–16377.
46 K. Taniguchi, H. Okumura, M. Honda, M. Suda, S. Fujinami, A. Kuwae, K. Hanai, S. Maeda and K. Kunimoto, *X-ray Struct. Anal. Online*, 2009, **25**, 93–94.
47 G. M. Sheldrick, *Acta Crystallogr., Sect. A: Found. Crystallogr.*, 2015, **71**, 3–8.
48 G. M. Sheldrick, *Acta Crystallogr., Sect. C: Struct, Chem.*, 2015, **71**, 3–8.
49 O. V. Dolomanov, L. J. Bourhis, R. J. Gildea, J. A. K. Howard and H. Puschmann, *J. Appl. Crystallogr.*, 2009, **42**, 339–341.
50 P. R. Spackman, M. J. Turner, J. J. McKinnon, S. K. Wolff, D. J. Grimwood, D. Jayatilaka and M. A. Spackman, *J. Appl. Crystallogr.*, 2021, **54**, 1006–1011.
51 J. Zhang, J. Jin, H. Xu, Q. Zhang and W. Huang, *J. Mater. Chem. C*, 2018, **6**, 3485–3498.
52 Y. Li, T. Ren and W. J. Dong, *J. Photochem. Photobiol., A*, 2013, **251**, 1–9.
53 R. S. Moog, D. D. Kim, J. J. Oberle and S. G. Ostrowski, *J. Phys. Chem. A*, 2004, **108**, 9294–9301.
54 O. A. Kucherak, L. Richert, Y. Mély and A. S. Klymchenko, *Phys. Chem. Chem. Phys.*, 2012, **14**, 2292–2300.
55 S. B. Yadav, S. Kothavale and N. Sekar, *J. Photochem. Photobiol., A*, 2019, **382**, 111937.
56 Y. Li, T. Tan, S. Wang, Y. Xiao and X. Li, *Dyes Pigm.*, 2017, **144**, 262–270.
57 P. S. Hariharan, E. M. Mothi, D. Moon and S. P. Anthony, *ACS Appl. Mater. Interfaces*, 2016, **8**, 33034–33042.
58 Y. Yang, B. Li and L. Zhang, *Sens. Actuators, B*, 2013, **183**, 46–51.
59 P. P. Gawas, A. Bora, R. P. Reji, B. Ramakrishna, P. B. Managutti, C. R. Göb, S. Mohamed, Y. Kawazoe, S. Velappa Jayaraman, Y. Sivalingam and V. Nutalapati, *J. Phys. Chem. C*, 2023, **127**, 6466–6482.
60 Q. Mei, L. Wang, B. Tian, F. Yan, B. Zhang, W. Huang and B. Tong, *New J. Chem.*, 2012, **36**, 1879–1883.
61 I. IUPAC, *'Compendium of Chemical Terminology' the ''Gold Book''*, Blackwell Scientific Publications, Oxford, 1997.
62 J. Bigler, Mercury Update: Impact of Fish Advisories. EPA Fact Sheet EPA-823-F-01–011, EPA, Office of Water, Washington, DC, 2001.

63 K. Kanagaraj, K. Bavanidevi, T. J. Chow and K. Pitchumani, *RSC Adv.*, 2014, **4**, 11714–11722.
64 P. K. Behera, T. Mukherjee and A. K. Mishra, *J. Lumin.*, 1995, **65**, 131–136.
65 Y. Long, H. Chen, H. Wang, Z. Peng, Y. Yang, G. Zhang, N. Li, F. Liu and J. Pei, *Anal. Chim. Acta*, 2012, **744**, 82–91.
66 D. Zhao and T. M. Swager, *Macromolecules*, 2005, **38**, 9377–9384.
67 N. S. Surajit Ghosh, S. Mandal, C. Banerjee and V. Govind Rao, *J. Phys. Chem. B*, 2012, **116**, 9482–9491.
68 S. Dhar, D. K. Rana, S. Singha Roy, S. Roy, S. Bhattacharya and S. C. Bhattacharya, *J. Lumin.*, 2012, **132**, 957–964.
69 L. D. Ward, *Methods Enzymol.*, 1985, **117**, 400–414.
70 H. S. Jung, T. Pradhan, J. H. Han, K. J. Heo, J. H. Lee, C. Kang and J. S. Kim, *Biomaterials*, 2012, **33**, 8495–8502.
71 Y. M. Bradford, S. Toro, S. Ramachandran, L. Ruzicka, D. G. Howe, A. Eagle, P. Kalita, R. Martin, S. A. T. Moxon, K. Schaper and M. Westerfield, *ILAR J.*, 2017, **58**, 4–16.
72 S. Cassar, I. Adatto, J. L. Freeman, J. T. Gamse, I. Iturria, C. Lawrence, A. Muriana, R. T. Peterson, S. Van Cruchten and L. I. Zon, *Chem. Res. Toxicol.*, 2020, **33**, 95–118.
73 B. Siddhardha, M. Dyavaiah and A. Syed, *Model Organisms for Microbial Pathogenesis, Biofilm Formation and Antimicrobial Drug Discovery*, 2020.